general Pol II transcription factors[7,20,25,26]. All protein fractions were dialysed against buffer B (25 mM Tris-HCl, pH 7.9, 50 mM KCl, 0.5 mM dithiothreitol, 0.1 mM EDTA and 20% glycerol (v/v)). 25-μl reactions contained either 25 ng 17M/5pAL7 and pG1 (ref. 5) or 100 ng pTEF(Δ-138) or pTEF(Δ-138$_{TATA}$)[15], with aliquots of TFTC, TFIIDβ and recombinant TBP[5]. Where indicated, 200 ng purified anti-TBP monoclonal antibody 1C2 was also included in the reactions before the other factors were added. GAL-VP16-activated transcription was performed as described[5]. After the preincubation steps (30 min), transcription was initiated by addition of nucleoside triphosphates to 0.5 mM and MgCl$_2$ to 5 mM. Transcriptions were incubated at 25 °C for 45 min. Correctly initiated transcripts from the different promoters were analysed by quantitative S1 nuclease analysis[15,27].

DNase I footprinting. DNase I footprinting was performed as described[18,19]. The labelled AdMLP-containing probes were amplified by polymerase chain reaction on either the 17M5/pAL7 (ref. 28) (Fig. 3a) or the pM677 (ref. 29) (Fig. 3b) templates. For the footprinting experiments, ten times more TBP, TFIIDβ, and TFTC was used than in the transcription reactions.

Received 4 December 1997; accepted 6 March 1998.

1. Zawel, L. & Reinberg, D. Common themes in assembly and function of eukaryotic transcription complexes. *Annu. Rev. Biochem.* **64,** 533–561 (1995).
2. Roeder, R. G. The role of general initiation factors in transcription by RNA polymerase II. *Trends Biochem. Sci.* **21,** 327–335 (1996).
3. Verrijzer, C. P. & Tjian, R. TAFs mediate transcriptional activation and promoter selectivity [see comments]. *Trends Biochem. Sci.* **21,** 338–342 (1996).
4. Chang, M. & Jaehning, J. A. A multiplicity of mediators: alternative forms of transcription complexes communicate with transcriptional regulators. *Nucleic Acids Res.* **25,** 4861–4865 (1997).
5. Brou, C. *et al.* Distinct TFIID complexes mediate the effect of different transcriptional activators. *EMBO J.* **12,** 489–499 (1993).
6. Jacq, X. *et al.* Human TAFII30 is present in a distinct TFIID complex and is required for transcriptional activation by the estrogen receptor. *Cell* **79,** 107–117 (1994).
7. Bertolotti, A., Lutz, Y., Heard, D. J., Chambon, P. & Tora, L. hTAFII68 a novel RNA/SSDNA-binding protein with homology to the pro-oncoproteins TLS/FUS and EWS is associated with both TFIID and RNA polymerase II. *EMBO J.* **15,** 5022–5031 (1996).
8. Mengus, G. *et al.* Cloning and characterization of hTAFII18, hTAFII20 and hTAFII28; three subunits of the human transcription factor TFIID. *EMBO J.* **14,** 1520–1531 (1995).
9. Lescure, A. *et al.* The N-terminal domain of human TATA-binding protein plays a role in transcription from TATA-containing RNA polymerase II and III promoters. *EMBO J.* **13,** 1166–1175 (1994).
10. Usheva, A. & Shenk, T. TATA-binding protein-independent initiation: YY1, TFIIB, and RNA polymerase II direct basal transcription on supercoiled template DNA. *Cell* **76,** 1115–1121 (1994).
11. Timmers, H. T. M., Meyers, R. E. & Sharp, P. A. Composition of transcription factor B-TFIID. *Proc. Natl Acad. Sci. USA* **89,** 8140–8144 (1992).
12. Van der Knaap, J. A., Willem Borst, J., van der Vliet, P. C., Gentz, R. & Timmers, H. T. M. Cloning of the cDNA for the TATA-binding protein-associated factor$_{II}$170 subunit of transcription factor B-TFIID reveals homology to global transcription regulators in yeast and *Drosophila*. *Proc. Natl Acad. Sci. USA* **94,** 11827–11832 (1997).
13. Hansen, S. K., Takada, S., Jacobson, R. H., Lis, J. T. & Tjian, R. Transcription properties of a cell type specific TATA-binding protein, TRF. *Cell* **91,** 71–83 (1997).
14. Crowley, T. E., Hoey, T., Liu, J. K., Jan, Y. N., Jan, L. Y. & Tjian, R. A new factor related to TATA-binding protein has highly restricted expression patterns in *Drosophila*. *Nature* **361,** 557–561 (1993).
15. Boam, D. S., Davidson, I. & Chambon, P. A TATA-less promoter containing binding sites for ubiquitous transcription factors mediates cell type-specific regulation of the gene for transcription enhancer factor-1 (TEF-1). *J. Biol. Chem.* **270,** 487–494 (1995).
16. Nakajima, N., Horikoshi, M. & Roeder, R. G. Factors involved in specific transcription by mammalian RNA polymerase II: purification, genetic specificity, and TATA box-promoter interactions of TFIID. *Mol. Cell. Biol.* **8,** 4028–4040 (1988).
17. Pugh, B. F. & Tjian, R. Transcription from a TATA-less promoter requires a multisubunit TFIID complex. *Genes Dev.* **5,** 1935–1945 (1991).
18. Purnell, B. A., Emanuel, P. A. & Gilmour, D. S. TFIID sequence recognition of the initiator and sequences further downstream in *Drosophila* class II genes. *Genes Dev.* **8,** 830–842 (1994).
19. Oelgeschlager, T., Chiang, C. M. & Roder, R. G. Topology and reorganization of a human TFIID-promoter complex. *Nature* **382,** 735–738 (1996).
20. Dubrovskaya, V. *et al.* Distinct domains of hTAF$_{II}$100 are required for functional interaction with transcription factor TFIIFb (RAP30) and incorporation into the TFIID complex. *EMBO J.* **15,** 3702–3712 (1996).
21. Ruppert, S. & Tjian, R. Human TAFII250 interacts with RAP74: implications for RNA polymerase II initiation. *Genes Dev.* **9,** 2747–2755 (1995).
22. Hisatake, K. *et al.* Evolutionary conservation of human TATA-binding-polypeptide-associated factors TAFII31 and TAFII80 and interactions of TAFII80 with other TAFs and with general transcription factors. *Proc. Natl Acad. Sci. USA* **92,** 85–89 (1995).
23. Lavigne, A. C. *et al.* Multiple interactions between hTAFII55 and other TFIID subunits. Requirements for the formation of stable ternary complexes between hTAFII55 and the TATA-binding protein. *J. Biol. Chem.* **271,** 774–780 (1996).
24. Lennon, G., Auffray, C., Polymeropoulos, M. & Soares, M. B. The I.M.A.G.E. Consortium: an integrated molecular analysis of genomes and their expression. *Genomics.* **33,** 151–152 (1996).
25. Gerard, M. *et al.* Purification and interaction properties of the human RNA polymerase B(II) general transcription factor BTF2. *J. Biol. Chem.* **266,** 20940–20945 (1991).
26. De Jong, J. & Roeder, R. G. A single cDNA, hTFIIA/alpha, encodes both the p35 and p19 subunits of human TFIIA. *Genes Dev.* **7,** 2220–2234 (1993).
27. Tora, L. *et al.* The human estrogen receptor has two independent nonacidic transcriptional activation functions. *Cell* **59,** 477–487 (1989).
28. Brou, C. *et al.* Different TBP-associated factors are required for mediating the stimulation of transcription *in vitro* by the acidic transactivator GAL-VP16 and the two nonacidic activation functions of the estrogen receptor. *Nucleic Acids Res.* **21,** 5–12 (1993).
29. Moncollin, V., Miyamoto, N. G., Zheng, X. M. & Egly, J. M. Purification of a factor specific for the upstream element of the adenovirus-2 major late promoter. *EMBO J.* **5,** 2577–2584 (1986).

Acknowledgements. We thank P. Chambon for support; J. C. Dantonel for help in identification and cloning of hTLF; E. Scheer for technical assistance; Y. Lutz for antibodies; D. Boam, V. Dubrovskaya, A. C. Lavigne, G. Mengus, I. Davidson and the IMAGE Consortium for reagents; H. T. M. Timmers for antibodies and for discussing unpublished results; A. Bertolotti for discussions; D. J. Heard for discussions and reading the manuscript; P. Eberling for peptide synthesis; the cell culture group for HeLa cells; R. Buchert, J.-M. Lafontaine and B. Boulay for illustrations; and A. Ozyhar for his contribution to the training of E.W. E.W. was supported by a fellowship from the Ministère de l'Enseignement Supérieur et de la Recherche. Research was supported by grants from the CNRS, the INSERM, the Hôpital Universitaire de Strasbourg, the Ministère de la Recherche et Technologie, the Fondation pour la Recherche Médicale and the Association pour la Recherche contre le Cancer.

Correspondence and requests for materials should be addressed to L.T. (e-mail: laszlo@titus.u-strasbg.fr).

corrections

Structure of the αβ tubulin dimer by electron crystallography

Eva Nogales, Sharon G. Wolf & Kenneth H. Downing

Nature **391,** 199–203 (1998)

In this Letter, the numbers for the secondary structure elements involved in Taxol binding are incorrect (page 202, second-to-last paragraph of main text). The sentences giving the correct numbers are, "In our model, the C-3′ is near the top of helix H1 (that is, between β:15–25), and the C2 group near H6 and the H6–H7 loop (that is, between β:212–222). The main interaction of the taxane ring is at L275, at the beginning of the B7–H9 loop." ☐

Spatial and temporal organization during cardiac fibrillation

Richard A. Gray, Arkady M. Pertsov & José Jalife

Nature **392,** 75–78 (1998)

The *x*-axis of Fig. 1d was mislabelled: the frequency values should instead read 0, 10, 20, 30, 40 Hz. ☐

Structure of the $\alpha\beta$ tubulin dimer by electron crystallography

Eva Nogales, Sharon G. Wolf* & Kenneth H. Downing

Life Science Division, Lawrence Berkeley National Laboratory, Berkeley, California 94720, USA

The $\alpha\beta$ tubulin heterodimer is the structural subunit of microtubules, which are cytoskeletal elements that are essential for intracellular transport and cell division in all eukaryotes. Each tubulin monomer binds a guanine nucleotide, which is nonexchangeable when it is bound in the α subunit, or N site, and exchangeable when bound in the β subunit, or E site. The α- and β-tubulins share 40% amino-acid sequence identity, both exist in several isotype forms, and both undergo a variety of post-translational modifications[1]. Limited sequence homology has been found with the proteins FtsZ[2] and Misato[3], which are involved in cell division in bacteria and *Drosophila*, respectively. Here we present an atomic model of the $\alpha\beta$ tubulin dimer fitted to a 3.7-Å density map obtained by electron crystallography of zinc-induced tubulin sheets. The structures of α- and β-tubulin are basically identical: each monomer is formed by a core of two β-sheets surrounded by α-helices. The monomer structure is very compact, but can be divided into three functional domains: the amino-terminal domain containing the nucleotide-binding region, an intermediate domain containing the Taxol-binding site, and the carboxy-terminal domain, which probably constitutes the binding surface for motor proteins.

In the presence of zinc ions, purified tubulin assembles into two-dimensional sheets that are ideal samples for electron crystallography studies[4]. In these sheets, protofilaments appear to be similar to those in microtubules, but associated in an antiparallel fashion. The zinc-induced tubulin sheets used here are cold-labile and require GTP for assembly. Addition of taxol stabilizes the sheets against low-temperature depolymerization and ageing[4], an effect similar to that on microtubules. Taxol binds to a single site on the dimer in the sheets, near lateral contacts between protofilaments[5].

We have previously described three-dimensional density maps of tubulin at 6.5 and 4 Å (refs 5, 6). The present model has been built into a 3.7-Å map derived from a data set that includes 93 electron-diffraction patterns (providing structure factor amplitudes) and 159 images (providing experimental phases). Table 1 and Fig. 1 summarize the data. The high quality of the phases produced a clean map, with well defined connectivity, which is readily interpretable in terms of secondary-structure elements. The present model of tubulin has been built in the raw density map without refinement and includes all but the last 10 and 18 C-terminal residues of α- and β-tubulin, respectively. Figure 2 shows the density map and the model in several regions of the dimer.

The density maps for α- and β-tubulin are almost superimposable. Differences are limited to the length and conformation of some loops, very slight displacements ($\sim$1 Å) of some of the secondary-structure elements, and differences in side-chain densities. Owing to the similarity between monomers, our description and comments on the model apply to both α- and β-tubulin unless indicated otherwise. Residue numbers correspond to the aligned sequences of α- and β-tubulin as shown in Fig. 3, and include gaps in the sequence of β-tubulin.

Figure 4 shows the ribbon diagram of the tubulin dimer model (see later for 'dimer' definition). The core of the structure contains two β-sheets of 6 and 4 strands, flanked by 12 α-helices. Although there is no clear division of the density into domains in the map, it makes sense functionally to divide the structure of each monomer into three sequential domains.

The N-terminal domain includes residues 1–205 and forms a Rossmann fold, which is typical of nucleotide-binding proteins, in which parallel β-strands alternate with α-helices. Helices H1 and H2 are on one side of the sheet, whereas helices H3, H4 and H5 are on the other. Strands B2 and B3 are poorly defined in the unrefined density map. The residues in the loops connecting H1 and B2, and H2 and B3, are included for completeness, but were built in very weak density. These segments are long predicted loops on the putative inside surface of the microtubule, and correspond to a region of the sequence that can accommodate insertions and deletions[7].

Strand B6 leads to the intermediate domain, residues 206–381, containing a mixed β-sheet and five surrounding helices. The domain starts with helices H6 and H7, followed by a long loop and helix H8 at the longitudinal interface between monomers. B7 is a long β-strand that interacts with the β-sheet in the N-terminal domain. The loop connecting B7 and H9 is more ordered in α-tubulin, where it is involved in strong lateral contacts. Following a long loop

Table 1 Electron crystallographic data

Two-dimensional crystals	
Two-sided plane roup	$P12_1$
Unit cell	$a = 80, b = 92$ Å
Sampling thickness	$c = 90$ Å
Sample thickness	62 Å
Experimental data set	
Resolution cut-off	3.7 Å
Number of structure factors	12,000
Electron diffraction	
Number of patterns by tilt angle	18 (0°), 57 (45°), 19 (55°)
R_{sym}	19%
R_{merge}	25%
Image/phase data	
Number of images by tilt angle	12 (0°), 51 (45°), 86 (60°)
Phase residual by resolution zones	36° (5–4 Å), 46° (4–3.7 Å)

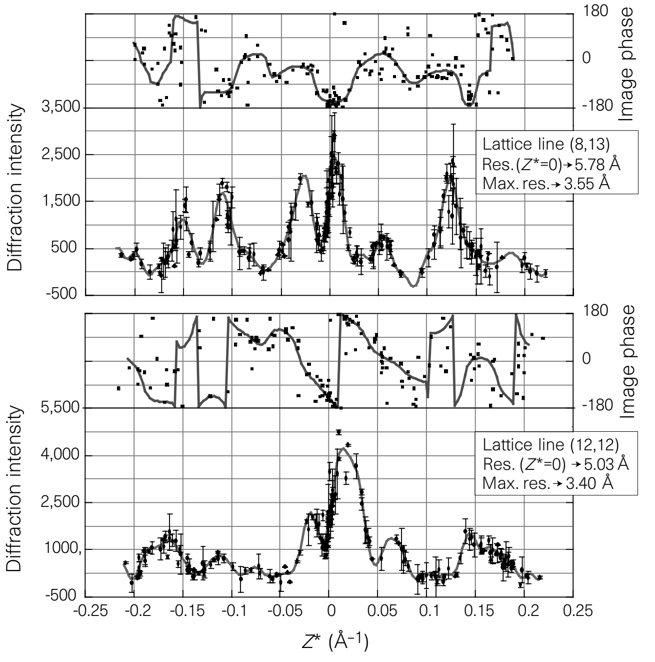

Figure 1 Experimental phase and intensity data and fitted curves for two representative reciprocal lattice lines. Error bars for the intensities are Friedel-pair differences. The resolution of each lattice line at the equator ($z^* = 0$) and its furthest point are indicated.

---

* Present address: Electron Microscopy Unit, Weizmann Institute of Science, Rehovot 76100, Israel.

come B8 and H10, which unravels at its C terminus in α-tubulin, followed by a very well defined short loop into B9. Finally, the loop between B9 and B10 includes an 8-residue insertion in the α-subunit which occludes the site that in β is occupied by taxol. The present model is compatible with the observation that C241 and C356 in the β-subunit can be crosslinked[8] (~8 Å apart in the model; Fig. 4b).

The C-terminal domain is formed by helices H11 and H12. These helices overlay the previous domains, sitting on the surface of the molecule that we have identified as the outside surface in the microtubule[9] (Fig. 4, legend). They are probably involved in the binding of MAPs and motor proteins. The loop connecting H11 and H12 is important for the interaction with the next monomer along the protofilament.

The last C-terminal residues of each monomer, missing from the model, correspond to the hypervariable part of the sequence where most of the differences between isotypes and across species occur. As the tubulin preparation we used included several α and β isotypes that are found in bovine brain, the inhomogeneity of the sample could contribute to the poor visibility in this part of the map. However, we do not see any significant difference in projection maps among αβIII, αβII, and undifferentiated tubulin (our unpublished results). This tubulin segment is highly acidic in both monomers and likely to be disordered, irrespective of the isotype composition.

The nucleotide in tubulin is positioned at the base of the Rossmann fold. The B1–H1, B2–H2 and B3–H3 loops, and the glycine-rich B4–H4 loop, appear to contact the phosphates. The

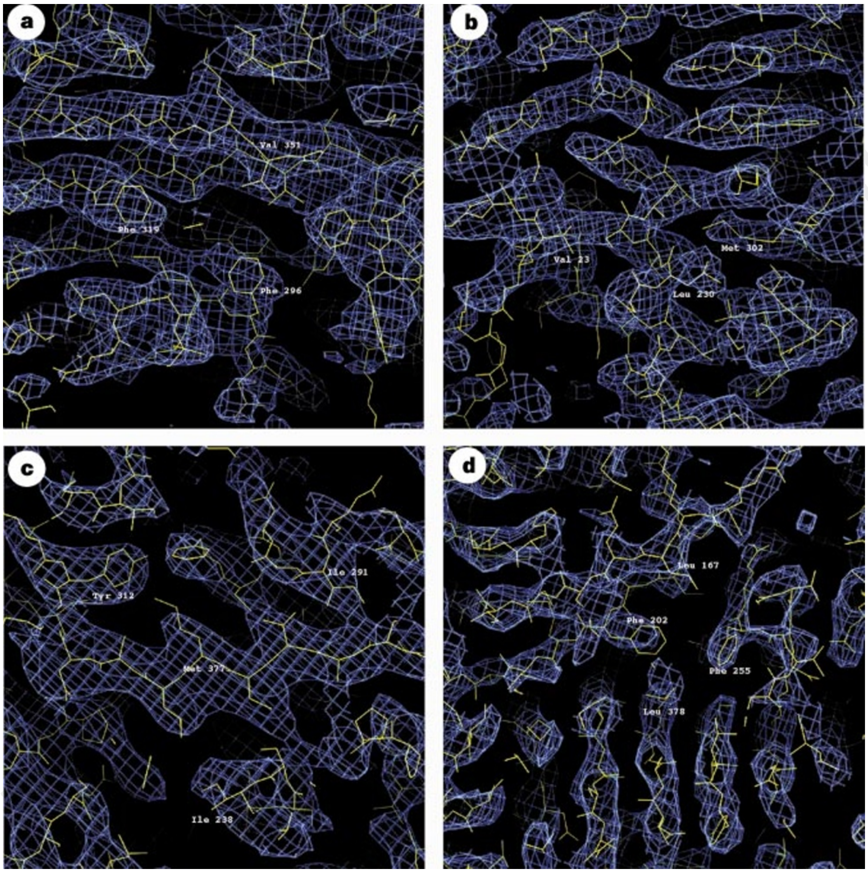

Figure 2 Sections of the experimental density map with the fitted model for different regions in the α- and β-tubulin molecules. **a**, **b**, Sections from β-tubulin; **c**, **d**, sections from α-tubulin. The map was calculated with a 3.7-Å cutoff. In the direction perpendicular to the crystals, the resolution is less than 3.7 Å, owing to the limit of 60° in tilt angle, but still sufficient that individual β-strands can be distinguished. The initial assignment of the sequence to the backbone trace was based mostly on the positions of aromatic side chains and on the connectivity of the density. Comparing corresponding densities in the α- and β-subunits, and relating the differences and similarities to those in their amino-acid sequences, were extremely helpful in tracing the chain. The sequence used for the model, in the absence of that from bovine brain tubulin, corresponds to porcine brain tubulin[28]. The numbering of residues is based on the alignment of the α- and β-tubulin sequences and so includes gaps in the sequence of β-tubulin (Fig. 3).

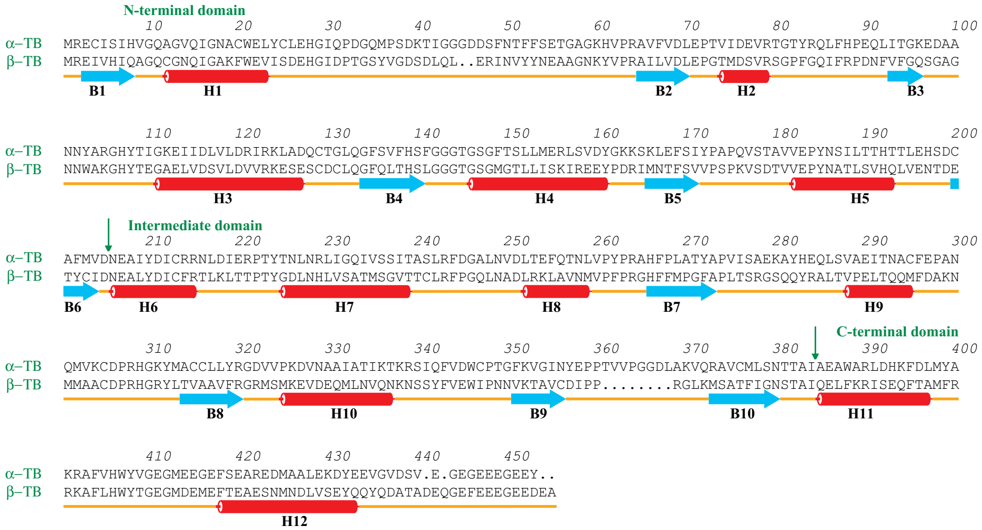

Figure 3 Sequences of pig brain α- and β-tubulin[28] used in the model (in the absence of tubulin sequences from cow we have used its closest known relative). Secondary structure elements are indicated and labelled as for Fig. 4. The tubulin preparations used in our experiments contained a mixture of isotypes. Most of the differences between isotypes are located at the extreme C terminus, which is not visible in our density. In most of the other positions of isotype differences, we arbitrarily chose the residue most similar to the other monomer.

B5–H5 loop is near the ribose, and N206 in H6, and Y224 and N228 in H7 interact with the nucleotide base. The position of the nucleotide agrees with models, based on comparison with other nucleotide-containing proteins, that position the phosphates near the glycine-rich loop. It is consistent with photocrosslinking experiments that locate C12 in β-tubulin near the guanine base[10], the peptide β157–176 near the ribose[11], and β65–79 by the γ-phosphate[12]. The position is also consistent with mutations in the region β105–111 affecting the hydrolysis of GTP[13]. Finally, C12 and either C203 or C213 can be crosslinked in β-tubulin, but only in the absence of the nucleotide[14]. In our model, the nucleotide is between those residues, but the distances between the cysteines are larger than 9 Å. However, the position of H6, containing C213, could easily be affected by the absence of nucleotide, bringing that cysteine closer to C12.

The nucleotide in one monomer interacts with the next monomer at the longitudinal interface. The interfaces between consecutive monomers in our density map are too similar to allow us to

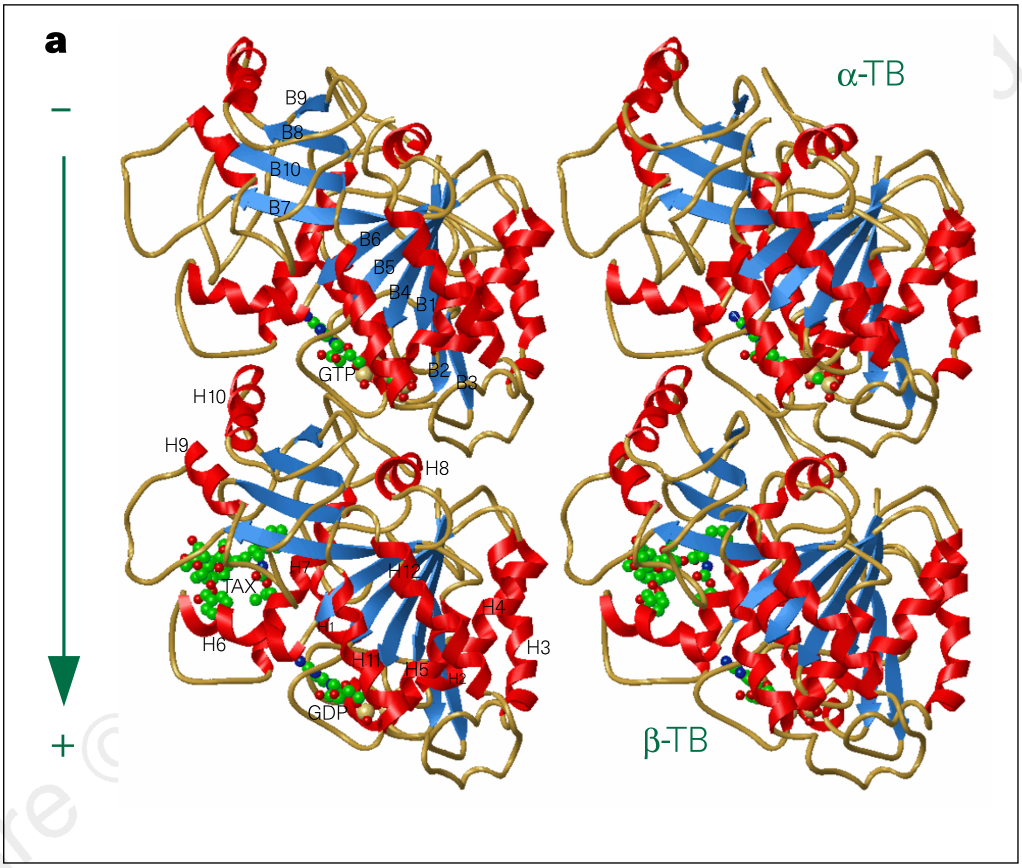

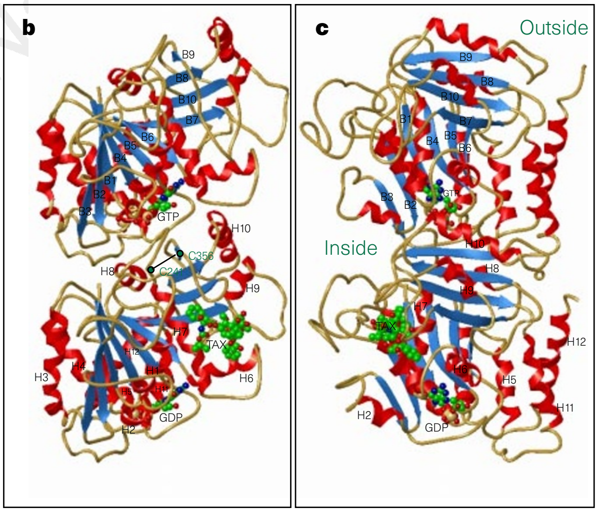

Figure 4 Ribbon diagram of the tubulin dimer showing α-tubulin with bound GTP (top), and β-tubulin containing GDP and taxotere (bottom). Labels for strands (in the α-subunit) and helices (in the β-subunit) are included. The arrow indicates the direction of the protofilament and microtubule axis. **a**, Stereo front view from the putative outside of the microtubule; **b**, back view from the putative inside of the microtubule; **c**, side view. Figures produced with AVS (Advanced Visual; ribbon module from M. Carson and A. Shah). The in-out orientation was determined by reference to reconstructions of intact microtubules[9]. Such reconstructions show prominent longitudinal ridge on the outside, which in our model would be formed by H11, H12 and the loop between H10 and B9, and shallow inside grooves giving the protofilament a bumpy appearance, corresponding in our model to H1, B3 and the long loops in the N-terminal domain. This represents the most likely arrangement of the dimer, because it buries the nucleotide that is at the non-exchangeable site in α (see text). For the nucleotide in β to be exchangeable at the plus end of a microtubule, the bottom of the figure would correspond to the plus end. We previously presumed the opposite orientation, based on a comparison of the zinc sheets in negatively stained, stain-glucose, and tannin-glucose embedding, with projection maps of open microtubules of known polarity in negative stain[9]. Some ambiguity in that determination may be introduced by uncertainty about the exact rotational alignment of the protofilament in the sheets with respect to those in open microtubules and by stain artefacts. The polarity with the plus end down would be consistent with experiments that located the β-subunit at the plus end of the microtubule[29] and the α-subunit at the minus end[30]. Circles in **b** indicate the positions of β Cys 241 and β Cys 356, separated by about 8 Å.

distinguish unequivocally between inter- and intradimer contacts (the interface near the N site is only slightly tighter than that by the E site). On the basis of the difference of exchangeability of nucleotide in the α and β monomers, we identified the intradimer interface as that in which the N site in the α-subunit is buried. The GTP at the E site in the β-subunit is partially exposed in the dimer but would be buried in the microtubule, where it becomes non-exchangeable. The assignment of the dimer shown in Fig. 4 thus provides the simplest explanation for nucleotide exchangeability in tubulin. Further support comes from data on the binding of colchicine. The main binding site of this drug is in the β-subunit, residues C356 and C241 (ref. 15) and region 1–36 (ref. 16) having been identified as part of the binding site (see the position of these residues in Fig. 4b). In addition, colchicine binds close to the $\alpha\beta$ intradimer interface[17]. On the other hand, antibodies against β241–256, near the top of the β-monomer (Fig. 4b), and to α214–226, at the bottom of the α-monomer, bind to the dimer but are unable to bind to the microtubule[18]. An alternative dimer to that shown in Fig. 4 would more readily explain these results, although the present model would be compatible if changes in the dimer occurred on binding to the microtubule.

On the basis of the similar behaviour of our sheets and microtubules, we believe that hydrolysis at the E site occurs upon sheet polymerization. In agreement with this, we find extra density in α-tubulin that corresponds to the γ-phosphate. The similarity between the two monomers, in spite of their being in two different nucleotide-bound states, is not surprising. The current model is that the GDP-containing dimer buried in the microtubule is kept locked in a GTP-like conformation by the microtubule lattice, and that only upon depolymerization does the GDP dimer 'spring' into a different conformation[19]. Comparison by electron microscopy of microtubules formed in the presence of GTP or of non-hydrolysable GTP analogues have shown only a change of 1.5 Å in the axial repeat (less than 2% of the subunit length)[20,21].

The favoured polymers for tubulin-GDP are rings formed by curved protofilaments[22]. The conformation of tubulin-GDP is thus referred to as 'curved', as opposed to the 'straight' conformation of tubulin-GTP (or tubulin-GDP held locked in the microtubule lattice)[23]. In two simplified models, the curved conformation could either be one in which longitudinal contacts between dimers are at an angle (consistent with the dimer definition in Fig. 4), or one in which the dimer is bent at the monomer–monomer interface (alternative dimer definition). A more general model would involve extensive allosteric effects following hydrolysis, which could affect points distant from the nucleotide-binding pocket.

Our study was done on tubulin sheets that were stabilized by taxol. The model in Fig. 4 includes a molecule of taxotere, a Taxol analogue whose structure has been solved by X-ray crystallography[24] (in taxotere, the C-10 acetyl and the C-3′ benzamide groups of Taxol have been replaced respectively by a hydroxyl and a N-t-BOC group). In our map, there is clear density for the taxane ring, the most dense and least flexible part of Taxol. Some density is also clear for one of the side chains. The position in the model is based on the best visual fit to the observed density. This position is in good agreement with photocrosslinking results placing the C-3′ group near the sequence β: 1–31 (ref. 25), and the C2 group near the sequence β: 217–231 (ref. 26). In our model, the group at C-3′ is near the top of helix H1 (that is, between β: 15–25), and the C2 group near H5 and the H5–H6 loop (that is, between β: 212–222). The main interaction of the taxane ring with tubulin is at L275, at the beginning of the B8–H9 loop.

Our model of tubulin shows a compact molecular structure with three functional domains: namely, GTP-binding, drug-binding and motor/MAP-binding domains. The interaction between domains is very tight, so the effects that nucleotides, drugs and other proteins in the cell have on tubulin are firmly linked. The assembly of tubulin and its regulation through dynamic instability results from the fine tuning of the three components. Knowledge of the structure of tubulin should be invaluable for understanding the microtubule system in the cell.

The structure of the bacterial FtsZ protein is reported in this issue[27]. Comparison of the tubulin and FtsZ models indicates that they have a common structural core of identical fold, which includes 10 β-strands surrounded by 10 α-helices: more detail will be revealed by careful comparison of there two structures. ☐

Methods

Crystalline tubulin sheets were polymerized in the presence of zinc from bovine brain tubulin (Cytoskeleton Inc.) and stabilized with taxol as described[4]. Samples were prepared by tannin–glucose embedding and examined at liquid-nitrogen temperature in a JEOL 4000 electron microscope at 400 kV following previously described procedures[4,5]. Images were taken using spot-scan imaging and dynamic focus correction. Images and electron diffraction patterns were processed and merged as described[4,9].

Received 8 August; accepted 27 October 1997.

1. Ludveña, R. F. The multiple forms of tubulin: different gene products and covalent modifications. *Int. Rev. Cyt.* **178,** 207–275 (1998).
2. Mukherjee, A. & Lutkenhaus, J. Guanine nucleotide-dependent assembly of FtsZ into filaments. *J. Bacteriol.* **176,** 2754–2758 (1994).
3. Gabor Miklos, G. L., Yamamoto, M., Burns, R. G. & Maleszka, R. An essential cell division gene of *Drosophila*, absent from *Saccharomyces*, encodes an unusual protein with tubulin-like and myosin-like peptide motifs. *Proc. Natl Acad. Sci. USA* **94,** 5189–5194 (1997).
4. Nogales, E., Wolf, S.G., Zhang, S. X. & Downing, K. H. Preservation of 2-D crystals of tubulin for electron crystallography. *J. Struct. Biol.* **115,** 199–208 (1995).
5. Nogales, E., Wolf, S. G., Khan, I. A., Ludueña, R. F. & Downing, K. H. Structure of tubulin at 6.5 Å and location of the taxol-binding site. *Nature* **375,** 424–427 (1995).
6. Nogales, E., Wolf, S. G. & Downing, K. H. Visualizing the secondary structure of tubulin: three-dimensional map at 4 Å. *J. Struct. Biol.* **118,** 119–127 (1997).
7. Burns, R. G. & Surridge, C. D. in *Microtubules* (eds Hyams, J. S. & Lloyd, C. W.) 3–32 (Wiley, New York, 1993).
8. Little, M. & Ludueña, R. F. Structural differences between brain β1- and β2-tubulins: implications for microtubule assembly and colchicine binding. *EMBO J.* **4,** 51–56 (1985).
9. Wolf, S. G., Nogales, E., Kikkawa, M., Gratzinger, D., Hirokawa, N. & Downing, K. H. Interpreting a medium-resolution model of tubulin: comparison of zinc-sheet and microtubule structure. *J. Mol. Biol.* **263,** 485–501 (1996).
10. Shivanna, B. D., Mejillano, M. R., Williams, T. D. & Himes, R. H. Exchangeable GTP binding site of β-tubulin—identification of cysteine 12 as the major site of cross-linking by direct photoaffinity labeling. *J. Biol. Chem.* **268,** 127–132 (1993).
11. Hesse, J., Thierauf, M. & Ponstingl, H. Tubulin sequence region β155–174 is involved in binding exchangeable guanosine triphosphate. *J. Biol. Chem.* **262,** 15472–15475 (1987).
12. Linse, K. & Mandelkow, E.-M. The GTP-binding peptide of β-tubulin. Localization by direct photoaffinity labeling and comparison with nucleotide-binding proteins. *J. Biol. Chem.* **263,** 15205–15210 (1988).
13. Davis, A., Sage, C. R., Dougherty, C. A. & Farrell, K. W. Microtubule dynamics modulated by guanosine triphosphate hydrolysis activity of β-tubulin. *Science* **264,** 839–842 (1994).
14. Little, M. & Ludueña, R. F. Location of two cysteines in brain β_1-tubulin that can be cross-linked after removal of exchangeable GTP. *Biochim. Biophys. Acta* **912,** 28–33 (1987).
15. Bai, R. *et al.* Identification of cysteine 354 of β-tubulin as part of the binding site for the A ring of colchicine. *J. Biol. Chem.* **271,** 12639–12645 (1996).
16. Uppuluri, S., Knipling, L., Sackett, D. L. & Wolff, J. Localization of the colchicine-binding site of tubulin. *Proc. Natl Acad. Sci. USA* **90,** 11598–11602 (1993).
17. Shearwin, K. E. & Timasheff, S. N. Effect of colchicine analogs on the dissociation of $\alpha\beta$ tubulin into subunits: the locus of colchicine binding. *Biochemistry* **33,** 894–901 (1994).
18. Andreu, J. M. Site-directed antibodies to tubulin. *Cell Motil. Cytoskel.* **26,** 1–6 (1993).
19. Caplow, M., Ruhlen, R. L. & Shanks, J. The free energy of hydrolysis of a microtubule-bound nucleoside triphosphate is near zero: all of the free energy for hydrolysis is stored in the microtubule lattice. *J. Cell Biol.* **127,** 779–788 (1994).
20. Vale, R. D., Coppin, C. M., Malik, F., Kull, F. J. & Milligan, R. A. Tubulin GTP hydrolysis influences the structure, mechanical properties, and kinesin-driven transport of microtubules. *J. Biol. Chem.* **269,** 23769–23775 (1994).
21. Hyman, A. A., Chrétien, D., Arnal, I. & Wade, R. H. Structural changes accompanying GTP hydrolysis of microtubules: information from a slowly hydrolyzable analog guanylyl-(α,β)-methylene-diphosphonate. *J. Cell Biol.* **128,** 117–125 (1995).
22. Díaz, J. F., Pantos, E., Bordas, J. & Andreu, J. M. Solution structure of GDP-tubulin double rings to 3 nm resolution and comparison with microtubules. *J. Mol. Biol.* **238,** 214–225 (1994).
23. Mandelkow, E. & Mandelkow, E.-M. Microtubules and microtubule-associated proteins. *Curr. Opin. Cell Biol.* **7,** 72–81 (1995).
24. Gueritte-Voegelein, F. *et al.* Structure of a synthetic taxol precursor: *N*-tert-butoxycarbonyl-10-deacetyl-*N*-debenzoyltaxol. *Acta Crystallogr. C* **46,** 781–784 (1990).
25. Rao, S., Krauss, N. E., Heerding, J. M., Orr, G. A. & Horwitz, S. B. 3′-(*p*-Azidobenzamido)taxol photolabels the N-terminal 31 amino acids of β-tubulin. *J. Biol. Chem.* **269,** 3132–3134 (1994).
26. Rao, S., Orr, G. A., Chaudhary, A. G., Kingston, D. G. I. & Horwitz, S. B. Characterization of the taxol binding site on the microtubule. *J. Biol. Chem.* **270,** 20235–20238 (1995).
27. Löwe, J. Y. & Amos, L. A. Crystal structure of the bacterial cell-division protein FtsZ complexed with GDP. *Nature* **391,** 203–206 (1998).
28. Ponstingl, H., Krauhs, E., Little, M., Kempf, T., Hofer-Warbinek, R. & Ade, W. Amino acid sequence of α- and β-tubulins from pig brain: heterogeneity and regional similarity to muscle proteins. *Cold Spring Harbor Symp. Quant. Biol.* **46,** 191–197 (1982).
29. Mitchison, T. J. Localization of an exchangeable GTP binding site at the plus end of microtubules. *Science* **261,** 1044–1047 (1993).

30. Fan, J., Griffiths, A. D., Lockhart, A., Cross, R. A. & Amos, L. A. Microtubule minus ends can be labeled with a phage display antibody specific to α-tubulin. *J. Mol. Biol.* **259,** 325–330 (1996).

Acknowledgements. We thank R. F. Ludueña for isotypically purified αβII and αβIII tubulin, M. Le for help with electron diffraction processing, and R. M. Glaeser and Y. L. Han for comments on the manuscript. Taxol was provided by the Drug Synthesis and Chemistry Branch, Division of Cancer Treatment of the National Cancer Institute. This work was supported by the NIH.

Correspondence and requests for materials should be addressed to E.N. Coordinates referred to in this Letter have been deposited in the Brookhaven Protein Data Bank with ID 1tub and will be accessible within one year.

Crystal structure of the bacterial cell-division protein FtsZ

Jan Löwe & Linda A. Amos

MRC Laboratory of Molecular Biology, Cambridge CB2 2QH, UK

Bacterial cell division ends with septation, the constriction of the cell wall and cell membranes that leads to the formation of two daughter cells[1,2]. During septation, FtsZ, a protein of relative molecular mass 40,000 which is ubiquitous in eubacteria and is also found in archaea and chloroplasts[3], localizes early at the division site to form a ring-shaped septum. This septum is required for the mechanochemical process of membrane constriction[4]. FtsZ is a GTPase[5,6] with weak sequence homology to tubulins[7]. The nature of FtsZ polymers *in vivo* is unknown, but FtsZ can form tubules, sheets and minirings *in vitro*[8,9]. Here we report the crystal structure at 2.8 Å resolution of recombinant FtsZ from the hyperthermophilic methanogen *Methanococcus jannaschii*. FtsZ has two domains, one of which is a GTPase domain with a fold related to one found in the proteins p21^{ras} and elongation factor EF-Tu. The carboxy-terminal domain, whose function is unknown, is a four-stranded β-sheet tilted by 90° against the β-sheet of the GTPase domain. The two domains are arranged around a central helix. GDP binding is different from that typically found in GTPases and involves four phosphate-binding loops and a sugar-binding loop in the first domain, with guanine being recognized by residues in the central connecting helix. The three-dimensional structure of FtsZ is similar to the structure of α- and β-tubulin[10].

Two FtsZ genes (named after filamenting temperature-sensitive mutant Z) from the archaeon *M. jannaschii* have been characterized by the genome project[11]. One gene, MJ0370, was amplified by genomic polymerase chain reaction (PCR) and expressed in *E. coli*/C41, a mutant of BL21 capable of expressing toxic genes[12]. Proteolysis during cell disruption was minimized by using heat-shock treatment. Cubic crystals were obtained and the structure was solved by multiple isomorphous replacement and density modification (see Methods and Table 1). The model (Fig. 1) contains residues 23–356, 116 water molecules, and one molecule of GDP; weak density for residues 1–22 was visible as an extension from helix H0.

FtsZ consists of two domains with a long, 23-residue, helix H5 (Figs 1a, 2) connecting them. The N-terminal portion of the molecule, containing residues 38–227, has GDP obtained from the expression host bound to it and will be called the GTPase domain. It consists of a six-stranded parallel β-sheet surrounded by two and three helices on both sides. The overall fold of the GTPase domain of FtsZ is related to typical GTPases and can be superimposed on the p21^{ras}–GDP complex (Protein Data Bank (PDB) entry 1Q21; ref. 13) using 52 Cα atoms (S1, H1, S2, H2, S4, H3 and S5) to give a root-mean-squared (r.m.s.) deviation of 1.88 Å. The topology of the β-sheet in FtsZ is 321456, which is slightly different from the topology in p21^{ras} (ref. 13), where it is 231456, but, together with the arrangement of five helices (H1, HL1, H2, H3 and H4), is consistent with typical Rossmann-fold topology[14]. Helix H2A is unique to FtsZ. Numbering of secondary structure elements (Fig. 2) follows the corresponding elements of p21^{ras} proteins.

The C-terminal domain, spanning residues 228–356, consists of a mainly parallel four-stranded central β-sheet supported by two helices on one side. The topology of the sheet is 1423, with strand 4 antiparallel to the others. The uncovered side of the sheet makes contacts with helix H5 and is otherwise open to the solvent. The fold of the C-terminal domain is related to chorismate mutase of *Bacillus subtilis* and can be superimposed on PDB entry 1COM[15] with an r.m.s. deviation of 1.83 Å over 52 Cα atoms (SC1, HC2, SC2, HC3, SC3 and SC4). Additionally, sequence comparisons give similarities to calmodulins in three loop regions (Swissprot CALM-TRYCR; loops between H5/HC1, SC1/HC2, and SC2/HC3) and to adenylyl cyclase (CYA1_HUMAN; residues 620–740), making a role in calcium binding feasible. The electrostatic potential on the

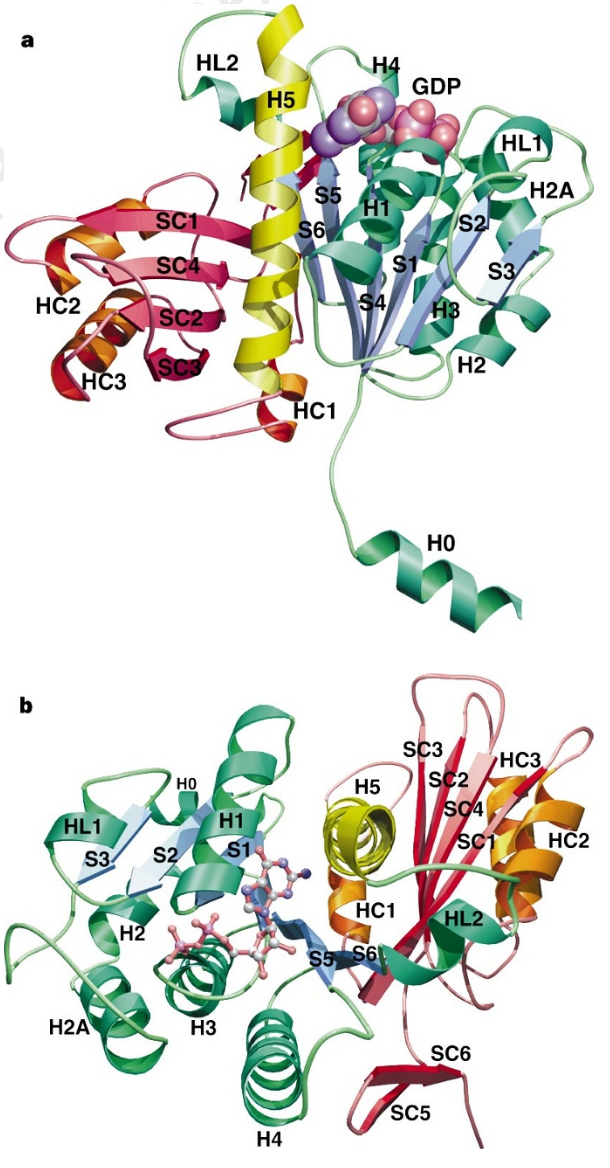

Figure 1 Ribbon drawings of FtsZ (residues 23–356) from *M. jannaschii*. **a**, View showing the GTPase domain in blue/green, the C-terminal domain in red/orange, and the connecting helix H5 in yellow. GDP is represented by a space-filling model. **b**, View of FtsZ rotated by ~90° from that in **a**. GDP is represented by a ball-and-stick model. Figures were prepared with POVSCRIPT (D. Peisach, personal communication)[28].

bootstrap replicates. ML analyses of these two trees showed that they are not significantly different.

Effects of long-branch taxa. To identify taxa with long apparent branch lengths, we performed a four-taxon NJ analysis (using gamma-corrected Kimura distances) using *Tripedalia* (a diploblast), *Antedon* (a deuterostome) and *Glycera* (a protostome) with each nematode taxon in turn. We recorded the inferred distance from the protostome–nematode node to the nematode taxon. MP distances were derived from the phylogeny presented in Fig. 1. These long-branch-length taxa often have extreme base-composition biases, but not all taxa with extreme base compositions have long branch lengths (for example, *Brugia* has an AT content of 79% but one of the shorter inferred branch lengths). NJ and MP analyses were re-performed with successive trimming of the long-branch taxa (distance >0.19 from root in four-taxon NJ analysis) from the dataset. As would be expected[29], exclusion of these taxa had effects on the bootstrap support for some clades. In particular, re-analysis excluding one or all of *Panagrellus*, *Panagrolaimus*, and *Strongyloides* yielded stronger bootstrap support for the cephalobid–steinernematid clade IV ($<50\%$ to 68%), and analyses excluding the long-branch rhabditid taxa *Bunonema*, *Teratorhabditis* and *Pellioditis* gave increased support for the Diplogasterida–Rhabditina clade V (51% to 93%). Figure 2a shows a consensus of these analyses: branchpoints that were supported by $>60\%$ in bootstrap long-branch taxa resampling of NJ or MP trees from the trimmed datasets were accepted. When there was no support for a resolved branching order, we collapsed nodes to form polytomies. Major clades supported by all analytical methods are shown and are numbered I–V. The association of Secernentea (clades II, IV and V) with the Plectidae has not been unequivocally resolved and is shown as a polytomy. We could not place the long-branch-length taxa in our trees with any certainty. We assessed statistical support for the placement of the vertebrate-parasitic taxa into four clades by calculating ML values for six-taxon subsets from the data. Each of the placements was strongly supported.

Received 16 July; accepted 12 December 1997.

1. Luc, M., Sikora, R. A. & Bridge, J. *Plant Parasitic Nematodes in Tropical and Subtropical Agriculture* (CAB International, Wallingford, UK, 1990).
2. Anderson, R. C. *Nematode Parasites of Vertebrates. Their Development and Transmission* (CAB International, Wallingford, UK, 1992).
3. Lambshead, J. Recent developments in marine benthic biodiversity research. *Oceanis* **19,** 5–24 (1993).
4. Riddle, D., Blumenthal, T., Meyer, B. & Priess, J. (eds) *C. elegans II* (Cold Spring Harbor Laboratory Press, NY, 1997).
5. Ellis, R. E., Sulston, J. E. & Coulson, A. R. The rDNA of *C. elegans*: sequence and structure. *Nucleic Acids Res.* **14,** 2345–2364 (1986).
6. Zarlenga, D. S., Stringfellow, F., Nobary, M. & Lichtenfels, J. R. Cloning and characterisation of ribosomal RNA genes from three species of *Haemonchus* (Nematoda: Trichostrongyloidea) and identification of PCR primers for rapid differentiation. *Exp. Parasitol.* **78,** 28–36 (1994).
7. Fitch, D. H. A., Bugaj-gaweda, B. & Emmons, S. W. 18S ribosomal gene phylogeny for some rhabditidae related to *Caenorhabditis elegans*. *Mol. Biol. Evol.* **12,** 346–358 (1995).
8. Baldwin, J. G., Frisse, L. M., Vida, J. T., Eddleman, C. D. & Thomas, W. K. An evolutionary framework for the study of developmental evolution in a set of nematodes related to *Caenorhabditis elegans*. *Mol. Phylogenet. Evol.* **8,** 249–259 (1997).
9. Baldwin, J. G. *et al.* The buccal capsule of *Aduncospiculum halicti* (Nemata: Diplogasterina): an ultrastructural and molecular phylogenetic study. *Can. J. Zool.* **75,** 407–423 (1997).
10. Swofford, D. L., Olsen, G. J., Waddell, P. J. & Hillis, D. M. in *Molecular Systematics* (eds Hillis, D. M., Moritz, C. & Mable, B. K.) 407–514 (Sinauer, Sunderland, MA, 1996)
11. Aguinaldo, A. M. A. *et al.* Evidence for a clade of nematodes, arthropods and other moulting animals. *Nature* **387,** 489–493 (1997).
12. Lorenzen, S. *The Phylogenetic Systematics of Free-Living Nematodes* (The Ray Society, London, 1994).
13. Malakhov, V. V. *Nematodes. Structure, Development, Classification and Phylogeny* (Smithsonian Institution Press, Washington, 1994).
14. Maggenti, A. R. in *Concepts in Nematode Systematics* (eds Stone, A. R., Platt, H. M. & Khalil, L. F.) 25–40 (Academic, London, 1983).
15. Baldwin, J. G. & Eddleman, C. D. Buccal capsule of *Zeldia punctata* (Nemata: Cephalobidae): an ultrastructural study. *Can. J. Zool.* **73,** 648–656 (1995).
16. Etzinger, A. & Sommer, R. The homeotic gene *lin-39* and the evolution of nematode epidermal cell fates. *Science* **278,** 452–455 (1997).
17. Poinar, G. Origins and phylogenetic relationships of the entomophilic rhabditids, *Heterorhabditis* and *Steinernema*. *Fund. Appl. Nematol.* **16,** 332–338 (1993).
18. Siddiqi, M. R. Phylogenetic relationships of the soil orders Dorylaimida, Mononchida, Triplonchida and Alaimida, with a revised classification of the subclass Enoplia. *Pak. J. Nematol.* **1,** 79–110 (1983).
19. Poinar, G. O. *The Natural History of Nematodes* (Prentice-Hall, Englewood Cliffs, NJ, 1983).
20. De Ley, P., van de Velde, M. C., Mounport, D., Baujard, P. & Coomans, A. Ultrastructure of the stoma in Cephalobidae, Panagrolaimidae and Rhabditidae, with a proposal for a revised stoma terminology in Rhabditida. *Nematologica* **41,** 153–182 (1995).
21. Winnepenninckx, B. *et al.* 18S rRNA data indicate that Aschelminthes are polyphyletic in origin and consist of at least three distinct clades. *Mol. Biol. Evol.* **12,** 1132–1137 (1995).
22. Blaxter, M. L. *et al.* Genes expressed in *Brugia malayi* infective third stage larvae. *Mol. Biochem. Parasitol.* **77,** 77–96 (1996).
23. Swofford, D. L. *PAUP: Phylogenetic Analysis Using Parsimony, Version 3.1* (Illinois Natural History Society, Champaign, 1993).
24. Maddison, W. & Maddison, D. *MacClade v3.0* (Sinauer, Sunderland, MA, 1993).
25. Kumar, S., Tamura, K. & Nei, M. *MEGA: Molecular Evolutionary Genetics Analysis. Version 1.0* (Pennsylvania State Univ., 1993).
26. Van de Peer, Y., Rensing, S., Maire, U.-G. & De Wachter, R. Substitution rate calibration of small subunit ribosomal RNA identifies chlorarachniophyte nucleomorphs as remnants of green algae. *Proc. Natl Acad. Sci. USA* **93,** 7732–7736 (1996).
27. Van de Peer, Y. & De Wachter, R. TREECON for Windows: a software package for the construction and drawing of evolutionary trees for the Microsoft Windows environment. *Comput. Appl. Biosci.* **10,** 569–570 (1994).
28. Yang, Z. *Phylogenetic Analysis by Maximum Likelihood (PAML) Version 1.2* (Univ. California, Berkeley, 1996).
29. Felsenstein, J. Cases in which parsimony and compatibility methods will be positively misleading. *Syst. Zool.* **27,** 401–410 (1978).

Acknowledgements. We thank our colleages for donations of nematode material, and D. Swofford for use of prerelease versions of PAUP*4.0. This work was supported by grants from the Wellcome Trust, the Linnean Society of London, the Belgian National Fund for Scientific Research, the NSF, the NIH and the United States Department of Agriculture.

Correspondence and requests for materials should be addressed to M.L.B. (e-mail: mark.blaxter@ed.ac.uk).

Spatial and temporal organization during cardiac fibrillation

Richard A. Gray*†, Arkady M. Pertsov* & José Jalife*

* *Department of Pharmacology, SUNY Health Science Center, 766 Irving Avenue, Syracuse, New York 13210, USA*
† *Department of Biomedical Engineering and Department of Medicine Division of Cardiovascular Disease, University of Albama at Birmingham, 1670 University Blvd, Birmingham, Alabama 35294-0019, USA*

Cardiac fibrillation (spontaneous, asynchronous contractions of cardiac muscle fibres) is the leading cause of death in the industrialized world[1], yet it is not clear how it occurs. It has been debated whether or not fibrillation is a random phenomenon. There is some determinism during fibrillation[2,3], perhaps resulting from rotating waves of electrical activity[4–6]. Here we present a new algorithm that markedly reduces the amount of data required to depict the complex spatiotemporal patterns of fibrillation. We use a potentiometric dye[7] and video imaging[8,9] to record the dynamics of transmembrane potentials at many sites during

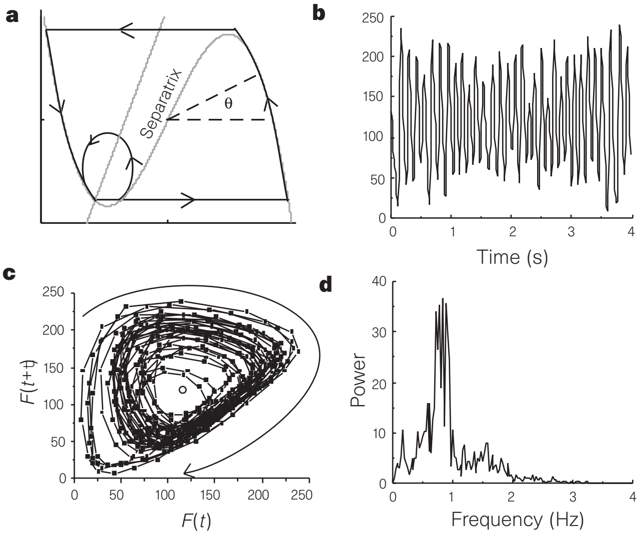

Figure 1 Temporal organization. **a**, Phase portrait of an excitable element incorporating two state variables[30]. A stable fixed point occurs at the intersection of the nullclines (dotted lines)[30]. **b**, Fluorescence signal (F) from a site on the surface of a rabbit heart during fibrillation. **c**, Phase portrait reveals trajectories circling around a centre (F_{mean}, F_{mean}), shown as a circle. **d**, The fluorescence signal exhibited a periodic component centred near 8 Hz, as observed in the corresponding power spectra. The frequency band 8 ± 3 Hz was different from equivalent white noise; $P < 0.00001$ for each heart (all sites combined).

fibrillation. Transmembrane signals at each site exhibit a strong periodic component centred near 8 Hz. This periodicity is seen as an attractor in two-dimensional-phase space and each site can be represented by its phase around the attractor. Spatial phase maps at each instant reveal the 'sources' of fibrillation in the form of topological defects, or phase singularities[10], at a few sites. Using our method of identifying phase singularities, we can elucidate the mechanisms for the formation and termination of these singularities, and represent an episode of fibrillation by locating singularities. Our results indicate an unprecedented amount of temporal and spatial organization during cardiac fibrillation.

It is still uncertain whether rotors underlie cardiac fibrillation. Self-organized rotors giving rise to spiral waves have been observed in various excitable media[11–13] including cardiac muscle[8]. Although stationary spiral waves occur in isolated thin pieces of cardiac tissue, in the whole heart, as in many excitable media, they tend to move throughout the heart. If these spiral waves move rapidly (at >30% of the wave speed), they give rise to fibrillatory activity[4]. The mechanisms of cardiac fibrillation vary[4,15], however, and fibrillation is usually the result of multiple three-dimensional electrical waves, sometimes described as meandering wavelets, propagating throughout the heart[16,17]. Cardiac fibrillation has been described in terms of

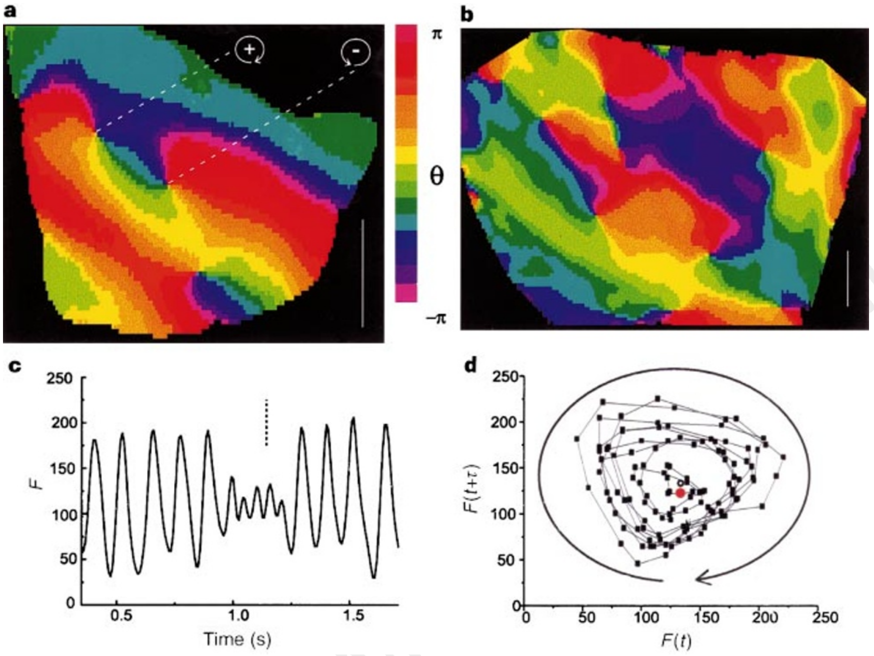

Figure 2 Snapshots of phase from the heart surface of the rabbit and sheep during sustained fibrillation. **a**, Rabbit; **b**, sheep. We classify rotor chirality as '+' for clockwise and '−' for anticlockwise[25]. At these instants, three phase singularities (two clockwise and one anticlockwise) were observed on the rabbit heart and nine (five clockwise and four anticlockwise) on the larger sheep heart. Signals (*F*) demonstrate (**c**) low amplitude and (**d**) remain near the centre of their phase portraits when a spatial phase singularity site is nearby. Dashed line and red circle indicate the time of the corresponding snapshot. Vertical white line represents 1 cm.

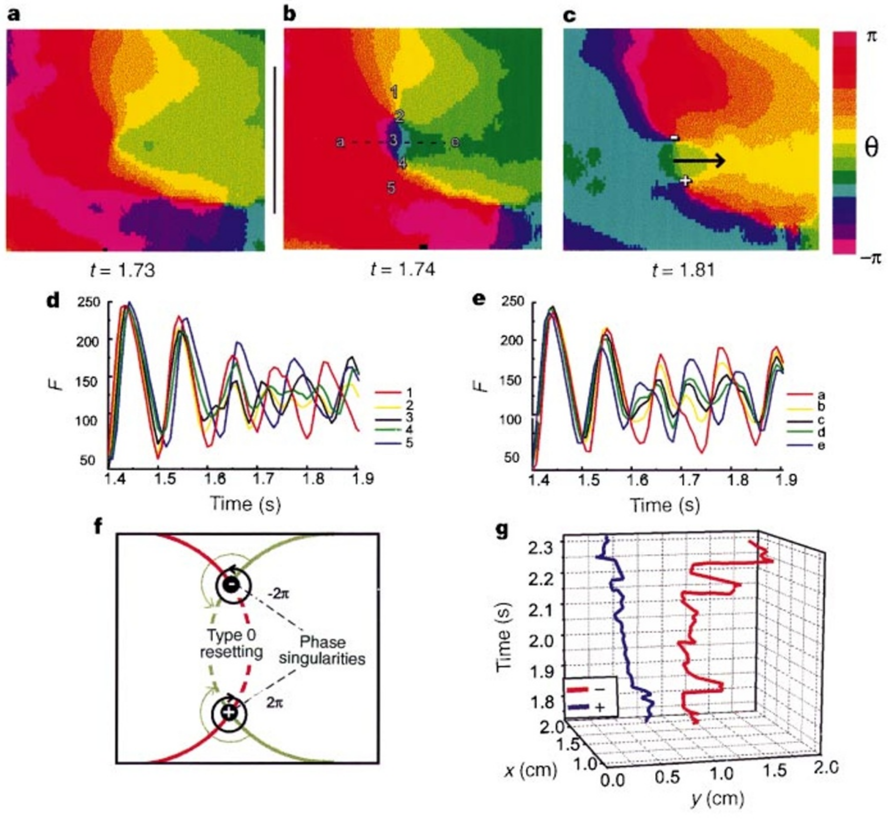

Figure 3 Initiation of a pair of spatial phase singularities. Snapshots of phase before (**a**), during (**b**), and after (**c**) the formation of a pair of spatial phase singularities during sustained fibrillation in the sheep heart. **d**, **e**, Transmembrane signals (F) measured at sites a–e and 1–5 labelled in **b**. **f**, A pair of singularities form when the local phase gradient becomes large (in other words, the excitation wave, $\theta \approx 0$ (green), approaches regions not fully recovered, $\theta \approx \pm\pi$ (red)). The excitation wave cannot proceed into the recovered region, and hence breaks, forming two phase singularities. The two excitation waves rotate around these newly formed singularities. Sustained rotation in the form of a pair of rotors occurs only if this excitation wave causes type 0, or even, phase resetting at the site of the initial wave break. Type 0 resetting (suprathreshold) advances the phase of this region into a new cycle, generating a new excitation wave (in the opposite direction to the previous wave; see arrow in **c**), resulting in the formation of a pair of self-sustaining rotors. Type 1 resetting (subthreshold) does not create this new excitation wave, and the phase singularity pair lasts less than one rotation. Notice the 'extra' cycle in the central region of block, sites 3 & c in **d** and **e**, indicative of type 0 resetting. **g**, Trajectories of '+' and '−' rotors following their initiation plotted in *x*, *y*, *t* space. Vertical line between **a** and **b** represents 1 cm.

rotors[4–6,14,15], on the basis of the long-held view that the heart is an example of a generic excitable medium[10,18–20]. There are many theories about fibrillation in excitable media, but only recently have experimental techniques become available to study the complex spatial patterns observed during sustained fibrillation[4,6,21–23]. Results from these experiments indicate that rotating waves are observed during fibrillation; however, they appear infrequently, and their initiation, termination and interaction have not been characterized.

An excitable element (for example, a cell, a patch of membrane, or a localized region in a spatially distributed system) can often be represented in phase space, which the element spends most of its time at a fixed point. A suprathreshold stimulus pushes the state of the excitable element past the separatrix and it continues along a closed-loop trajectory; however, if the stimulus is subthreshold, the state of the element does not cross the separatrix (Fig. 1). In periodic dynamics, it is simple and useful to represent the state of an element by its phase (θ) around the loop. The responses of single elements to external stimuli have been extensively studied by analysing the induced changes in θ (that is, phase resetting). Two fundamentally different responses to stimuli occur, namely, type 0 or even resetting, where a suprathreshold response gives rise to a new cycle, and type 1 or odd resetting, which effects a subthreshold response to stimuli[10,24]. In spatially extended excitable systems, the stimulation of individual elements are provided by neighbouring elements (usually through diffusion).

A rotor is composed of a wave of excitation propagating around a topological defect, which is known as a phase singularity. A spatial phase singularity is a site in an excitable medium at which the phase of the site is arbitrary; the neighbouring elements exhibit a continuous progression of phase that is equal to $\pm 2\pi$ around this site. As shown in Fig. 1, transmembrane signals (F) recorded from the surface of rabbit and sheep hearts during fibrillation exhibited attractors in reconstructed two-dimensional phase space, when $F(t)$ was plotted against $F(t+\tau)$ where t is time and τ is the embedding delay (see Methods). Periodicity of each site was near 8 Hz. Although trajectories for subsequent cycles did not coincide in phase space, the trajectories circulated around a central region, allowing us to construct a new variable, the phase along the attractor, θ. The phase variable (θ) calculated at each site rotated clockwise ($d\theta < 0$) 89 ± 4% of the time, indicating that the trajectories were encircling the centre. The distance of points from the centre was smaller for $d\theta \geq 0$ compared with $d\theta < 0$ ($P < 0.0001$), as would be expected if the phase were ambiguous at the centre[10]. This new variable, θ, has certain advantages over the fluorescence signal (F) that simplify the analysis of fibrillation. First, use of θ eliminates the need to pick activation times, which is difficult during fibrillation, especially in the important regions of slow propagation and block. Second, we can test directly whether spatial phase singularities exist and are necessary to maintain fibrillation.

With this new method to represent fibrillation by phase, $\theta(x, y, t)$, we could study directly the detailed dynamics of spatial phase singularities and rotors, including their initiation and termination. The spatial phase patterns during sustained fibrillation (Fig. 2) concurred with theoretical predictions (for example, isophase lines connect phase singularities of opposite chirality or end on a no-flux boundary)[10,25]. Spatial phase singularities are easily identified as sites at which all phase values ($-\pi$ to π) converge. The continuous spatial phase changes reflect waves propagating on the heart surface as a result of processes of excitation, recovery, and diffusion, and indicate that each site of the heart surface can be represented by its phase around a two-dimensional attractor. We elucidated the mechanism of rotor formation and termination by analysing successive frames of $\theta(x, y, t)$, (representative examples are shown in Figs 3 and 4). Movement of existing phase singularities created Doppler-shifted[4,8,26] short cycle lengths, and thus created large local phase gradients in front of moving singularities. The formation of phase singularities was necessary, although not sufficient, for sustained rotation (that is, for rotor formation). In addition to the formation of phase singularities, a new excitation wave must be generated[27] (that is, type 0 or even resetting must occur)[10,24] to form a rotor. Lifespan histograms for both rabbits and sheep indicate that the majority (80% for rabbit and 84% for sheep) of phase singularities lasted <100 ms, which is less than one rotation[4,14]. Therefore,

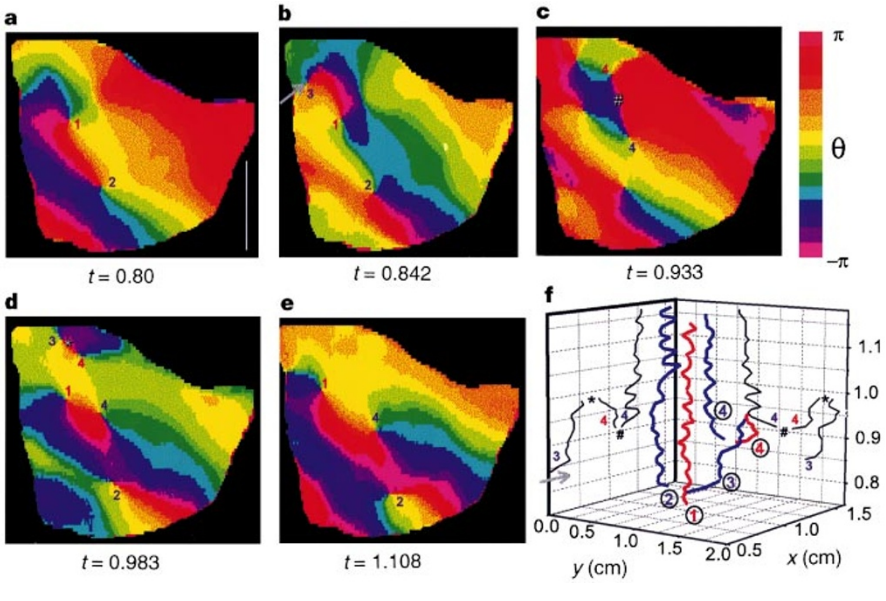

Figure 4 Dynamics of phase singularities. **a–e**, Snapshots of phase illustrating rotor dynamics on the surface of the rabbit heart during sustained fibrillation. **f**, Trajectories of the clockwise and anticlockwise rotors shown in **a–e** plotted in x, y, t space. Each rotor is numbered (1–4) and coloured (clockwise, blue; anticlockwise, red). The x and y projections in time are shown in black in **f** (except for rotors 1 and 2 for clarity). **a**, Rotors 1 and 2 formed separately before the time interval shown here (0.75–1.17 s). **b**, At t = 0.842 s a clockwise rotor (3) enters the field of view from the left and moves rapidly toward the right (grey arrow in **b** and **f**). This movement creates a convergence of phase values ahead of rotor 3, and (**c**) a pair of phase singularities (4) form (# in **c** and **f**) when the excitation wave ($\theta \approx 0$) reaches the high-phase-gradient region. Both of these newly formed singularities move; the clockwise one collides with anticlockwise-rotating rotor 3, resulting in mutual annihilation (asterisk in **d**), whereas the anticlockwise one survives in the form of a rotor. Vertical white line represents 1 cm.

only ~20% of phase singularities formed rotors.

Rotor termination occurred when rotors of opposite chirality merged or when a single rotor collided with a boundary (both of these occurrences are topologically equivalent for a non-flux boundary)[10]. Specifically, rotor pairs were mutually annihilated if the phase gradient between the rotors, perpendicular to the line connecting the phase singularities, was sufficiently large to stop propagation. On the basis of the number of rotors observed in our recording array, each rotor occupied on average $12 \pm 4\,\mathrm{cm}^2$. According to rough measurements of heart surface area, we estimate that the total number of rotors during fibrillation would be approximately 1–2 for rabbits, 5 for sheep, and 15 for humans (assuming the rotor density is the same in humans).

These results indicate that analysing the complex spatiotemporal patterns seen during fibrillation on the surface of the heart can be greatly simplified by identifying and analysing phase singularities. This analysis reveals topological restrictions to the dynamics of fibrillation[10]: first, phase lines do not intersect; second, phase singularities are joined via isophase lines to two other singularities with opposite chirality (or a boundary); and third, phase singularities form and terminate as oppositely rotating pairs (Fig. 4). Under certain conditions, phase singularities give rise to rotors, which sustain fibrillation. The direct observation of phase singularities has led, for the first time, to the quantification of fibrillation in terms of rotor number and lifespan, and to the elucidation of the mechanisms underlying the formation and termination of rotors. □

Methods

The experimental protocols, video imaging-recording system, and signal processing have been described previously[14,28]. We acquired video images (typically 200×100 pixels) from the ventricular surface at a rate of 120 frames s^{-1} ($\Delta t = 0.00833\,\mathrm{s}$). We applied spatial and temporal filtering to improve the signal-to-noise ratio[28]. Two-dimensional phase portraits were obtained by plotting $F(t)$ versus $F(t+\tau)$ (ref. 29), where $t + n\Delta t$ and n is the frame number. The value of τ was chosen to be roughly one-quarter of the cycle length during fibrillation ($\tau = 25\,\mathrm{ms}$); this value roughly corresponds to the first zero crossing of the autocorrelation of F, indicating linear independence. A new variable phase, $\theta(t)$, was computed as $\mathrm{atan}(F(t+\tau) - F_{\mathrm{mean}}, F(t) - F_{\mathrm{mean}})$. Isolated hearts from rabbits of ~3 kg ($n = 3$) and from sheep of ~20 kg ($n = 3$) body weight were maintained at 36–38 °C. Ventricular fibrillation was initiated by rapid pacing, and 4-s recordings were obtained at least 5 min after initiation (perfusion was maintained during fibrillation). In Figs 2–4, white and black bars near images reflect a distance of 1 cm. Values are presented as mean ± s.d.m. Comparisons were made with paired student t-tests.

Received 30 September; accepted 8 December 1997.

1. Myerburg, R. J. *et al.* in *Cardiac Electrophysiology, From Cell to Bedside* (W. B. Saunders, Philadelphia, 1990).
2. Garfinkel, A. *et al.* Quasiperiodicity and chaos in cardiac fibrillation. *J. Clin. Invest.* **99,** 305–314 (1997).
3. Witkowski, F. X. *et al.* Evidence for determinism in ventricular fibrillation. *Phys. Rev. Lett.* **75,** 1230–1233 (1995).
4. Gray, R,. A. *et al.* Mechanisms of cardiac fibrillation. *Science* **270,** 1222–1223 (1995).
5. Ikeda, T. *et al.* Mechanism of spontaneous termination of functional reentry in isolated canine right atrium. *Circulation* **94,** 1962–1973 (1996).
6. Lee, J. J. *et al.* Reentrant wavefronts in Wiggers' stage II ventricular fibrillation. *Circ. Res.* **78,** 660–675 (1996).
7. Salzberg, B. M., Davila, H. V. & Cohen, L. B. Optical recordings of impulses in individual neurons of an invertebrate central nervous system. *Nature* **246,** 508–509 (1973).
8. Davidenko, J. M., Pertsov, A. M., Salomonsz, R., Baxter, W. T. & Jalife, J. Stationary and drifting spiral waves of excitation in isolated cardiac muscle. *Nature* **355,** 349–351 (1991).
9. Pertsov, A. M., Davidenko, J. M., Salomonsz, R., Baxter, W. T. & Jalife, J. Spiral waves of excitation underlie reentrant activity in isolated cardiac muscle. *Circ. Res.* **72,** 631–650 (1993).
10. Winfree, A. T. *When Time Breaks Down.* (Princeton Univ. Press, 1987).
11. Winfree, A. T. Scroll-shaped waves of chemical activity in three dimensions. *Science* **181,** 937–939 (1973).
12. Goldbeter, A. Mechanism for oscillatory synthesis of cAMP in *Dictyostelium discoideum*. *Nature* **253,** 540–542 (1975).
13. Lechleiter, J., Girdad, S. & Peralta, E. Spiral calcium wave propagation and annihilation in *Xenopus laevis* oocytes. *Science* **252,** 123–125 (1991).
14. Gray, R. A. *et al.* Non-stationary vortex-like reentry as a mechanism of polymorphic ventricular tachycardia in the isolated rabbit heart. *Circulation* **91,** 2454–2469 (1995).
15. Winfree, A. T. Electrical turbulence in three-dimensional heart muscle. *Science* **266,** 1003–1006 (1994).
16. Moe, G. K. & Abildskov, J. A. Atrial fibrillation as a self-sustaining arrhythmia independent of focal discharge. *Am. Heart J.* **58,** 59–70 (1959).
17. Allessie, M. A., Lammers, W., Bonke, F. I. M. & Hollen, J. in *Cardiac Electrophysiology and Arrhythmias* 265–275 (Grune and Stratton, Orlando, 1985).
18. Krinsky, V. I. Mathematical models of cardiac arrhythmias (spiral waves). *Pharmacol. Ther. B* **3,** 539–555 (1978).
19. Zykov, V. S. *Simulation of Wave Processes in Excitable Media.* (University Press, New York/Manchester, 1987).
20. Gray, R. A. & Jalife, J. Spiral waves and the heart. *Int. J. Bifurc. Chaos* **6,** 415–435 (1996).
21. Bayly, P. V. *et al.* Efficient electrode spacing for examining spatial organization during ventricular fibrillation. *J. Cardiovasc. Electrophysiol.* **4,** 533–546 (1993).
22. Bove, R. T. & Dillon, S. M. A new high performance system for imaging cardiac electrical activity. *Circulation* **94,** I–714 (1996).
23. Cha, Y. M., Birgersdotter-Green, U., Wolf, P. L., Peters, B. B. & Chen, P. S. The mechanism of termination of reentrant activity in ventricular fibrillation. *Circ. Res.* **74,** 495–506 (1994).
24. Glass, L. & Mackay, M. C. *From Clocks to Chaos* (Princeton Univ. Press, 1988).
25. Agladze, K. I. & Krinsky, V. I. Multi-armed vortices in an active chemical medium. *Nature* **296,** 424–426 (1982).
26. Fast, V.G. & Pertsov, A. M. Drift of a vortex in the myocardium. *Biophysics* **35,** 489–494 (1990).
27. Gotoh, M. *et al.* Cellular graded responses and ventricular vulnerability to reentry by a premature stimulus in isolated canine ventricle. *Circulation* **95,** 2141–2154 (1997).
28. Gray, R. A., Ayers, G. & Jalife, J. Video imaging of atrial defibrillation in the sheep heart. *Circulation* **95,** 1038–1047 (1997).
29. Takens, F. in *Dynamical Systems and Turbulence* (eds Rand, D. A. & Young, L. S.) *Lecture Notes in Mathematics* **898,** 366–381 (Springer, Berlin, 1981).
30. Fitzhugh, R. Impulses and physiological states in theoretical models of nerve membrane. *Biophys. J.* **1,** 445–446 (1961).

Acknowledgements. We thank O. Berenfield, Z. Silverman, J. Jiang and M. Flanagan for technical assistance and M. Vinson for reading the manuscript. This work was supported by grants from the Whitaker Foundation and the N.I.H.

Correspondence and requests for materials should be addressed to R.A.G. (e-mail: rag@crml.uab.edu).

Spatiotemporal evolution of ventricular fibrillation

Francis X. Witkowski*, L. Joshua Leon†, Patricia A. Penkoske‡, Wayne R. Giles§, Mark L. Spano‖, William L. Ditto¶ & Arthur T. Winfree#

* *Department of Medicine, and ‡ Department of Surgery, University of Alberta, Edmonton, Alberta T6G 2R7, Canada*
† *Ecole Polytechnique, Montreal, Quebec H3C 3J7, Canada*
§ *Department of Physiology and Biophysics, University of Calgary, Calgary, Alberta T2N 4N1, Canada*
‖ *Naval Surface Warfare Center, West Bethesda, Maryland 20817, USA*
¶ *Applied Chaos Laboratory, School of Physics, Georgia Institute of Technology, Atlanta, Georgia 30332, USA*
\# *Department of Ecology and Evolutionary Biology, University of Arizona, Tucson, Arizona 85721, USA*

Sudden cardiac death is the leading cause of death in the industrialized world, with the majority of such tragedies being due to ventricular fibrillation[1]. Ventricular fibrillation is a frenzied and irregular disturbance of the heart rhythm that quickly renders the heart incapable of sustaining life. Rotors, electrophysiological structures that emit rotating spiral waves, occur in several systems that all share with the heart the functional properties of excitability and refractoriness. These re-entrant waves, seen in numerical solutions of simplified models of cardiac tissue[2], may occur during ventricular tachycardias[3,4]. It has been difficult to detect such forms of re-entry in fibrillating mammalian ventricles[5–8]. Here we show that, in isolated perfused dog hearts, high spatial and temporal resolution mapping of optical transmembrane potentials can easily detect transiently erupting rotors during the early phase of ventricular fibrillation. This activity is characterized by a relatively high spatiotemporal cross-correlation. During this early fibrillatory interval, frequent wavefront collisions and wavebreak generation[9] are also dominant features. Interestingly, this spatiotemporal pattern undergoes an evolution to a less highly spatially correlated mechanism that lacks the epicardial manifestations of rotors despite continued myocardial perfusion.

Ventricular fibrillation is a complicated, often lethal, but poorly understood, high-frequency mode of electrical activity. It can be